
Empirical radiation patterns as a method to assess crosstalk under scenarios of heterogeneous reference media

Mariana Lume, Ivan J. Sánchez G. and Kris Innanen

ABSTRACT

Analysis of radiation patterns is the most common method to evaluate crosstalk between parameters in Full Waveform Inversion problems. Typically, these are constructed from analytic expressions subject to not so realistic assumptions, such as the use of homogeneous reference media. This study focuses on introducing a workflow to extract the empirical radiation patterns from simulated scattered wavefields and on making use of it to assess the V_P , V_S and ρ scattering patterns generated from wavefields produced under different heterogeneous backgrounds. To achieve this, radius dependent masks to isolate displacements of interest and sweeps of angles were used. The proposed workflow is beneficial since it allows to extract highly accurate empirical patterns and demonstrates that, under heterogeneous scenarios, the shape of the radiation patterns has certain changes from what is theoretically expected, and that slightly different crosstalk regions from those indicated by the analytic expressions might occur, as well as sensitivity variations.

INTRODUCTION

Multiparameter Full Waveform Inversion (FWI) is a challenging problem because, depending on the parameterization, inter-parameter coupled effects or crosstalk can be introduced to the seismic response in a selected propagation regime, producing slow convergence and poor estimations. Crosstalk is a phenomenon that occurs when parameters of different classes are confused in the inversion. The most common strategy to mitigate these effects is to analyze the radiation patterns associated to a diffractor point in the model grid and choose a suitable parameterization that still describes the earth, but also produces their minimal overlap over the scattering angles (Operto et al. (2013); Keating and Innanen (2019)).

Radiation patterns provide information about the variations of amplitudes that the partial derivatives of the predicted data (used within the gradient in local optimization algorithms) experience with scattering angles (Operto et al., 2013). Moreover, when the scattering patterns of two parameter classes are similar, also are their gradient updates, being difficult to properly differentiate them during the inversion (Métivier et al., 2015).

Typically, analytic expressions of radiation patterns are calculated to perform crosstalk analysis for a particular parameterization and acquisition geometry. Generally, these expressions have been derived and published for different set of known parameters and/or wave equations (e.g., scalar acoustic, elastic, viscoelastic, among others) using a point scatterer model of a localized heterogeneity embedded in a homogeneous medium, assuming plane waves and working of the basis of the Born approximation to find the solution of the scattered wavefields (Sato (1984); Wu and Aki (1985); Sato et al. (2012); Kamath and Tsvankin (2016); Moradi and Innanen (2019)).

Therefore, the main objective of this study was to introduce a workflow that allows to

extract the empirical radiation patterns from simulated scattered P-P and P-S wavefields generated from a virtual source or scatter point of individual model perturbations, regardless the parameterization selected and if its analytic expressions are known or not. The workflow was tested by comparing the empirical and analytic scattering patterns produced by perturbations of P-wave velocity (V_P), S-wave velocity (V_S) and density (ρ) and the independence from analytic expressions was exploited by studying the radiation patterns upon scenarios of heterogeneous reference media in order to understand how the patterns change from the theoretic expectations and how crosstalk might vary in more realistic configurations that are not commonly addressed with analytic equations.

ANALYTIC RADIATION PATTERNS IN V_P , V_S AND ρ MODEL SPACE

The scattering theory explains that the actual medium that represents the subsurface and where a wave propagates results from the sum of a homogeneous background (reference medium) and small perturbations in model properties (Moradi and Innanen, 2015). For an isotropic elastic scenario, characterized by the density and Lamé coefficients (λ and μ) contained in a stress tensor C_{ij} , the following relationships hold:

$$\lambda(\mathbf{x}) = \lambda_0 + \delta\lambda(\mathbf{x}) = \lambda_0 [1 + \xi(\mathbf{x})] \quad (1)$$

$$\mu(\mathbf{x}) = \mu_0 + \delta\mu(\mathbf{x}) = \mu_0 [1 + \chi(\mathbf{x})] \quad (2)$$

$$\rho(\mathbf{x}) = \rho_0 + \delta\rho(\mathbf{x}) = \rho_0 [1 + \nu(\mathbf{x})] \quad (3)$$

where λ_0 , μ_0 , ρ_0 are the background model properties and λ , μ , ρ are the actual model properties. Additionally, the fractional fluctuations correspond to a localized heterogeneity (Figure 1) and must meet $|\xi|, |\chi|, |\nu| \ll 1$.

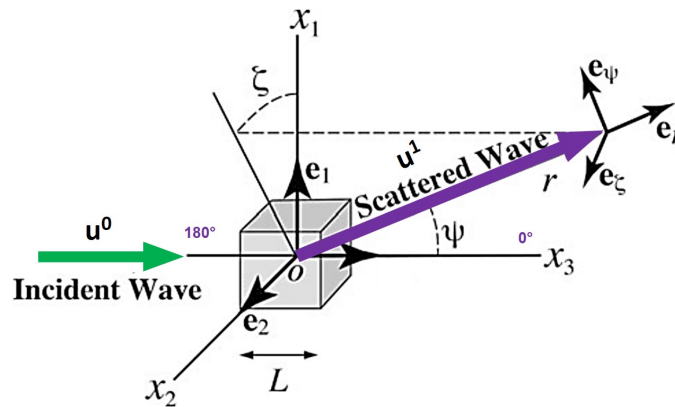


FIG. 1. Representation of a localized inhomogeneity of size L from which the scattered wavefield is generated. r , ψ , and ζ are spherical coordinates and \mathbf{e}_r , \mathbf{e}_ψ and \mathbf{e}_ζ are the unit base vectors in that system (Modified from Sato et al. (2012)).

In order to study a scattered wavefield and be able to extract its analytic radiation patterns, we can analyze a plane wave that interacts with a localized inhomogeneity or scatter point, using the first order perturbation method or Born approximation in stationary state (Sato et al., 2012). To obtain the P-P and P-S analytic radiation patterns we must start by considering:

$$\mathbf{u} = \mathbf{u}^0 + \mathbf{u}^1 \quad (4)$$

where \mathbf{u} is the total wavefield, \mathbf{u}^0 is the incident wavefield and \mathbf{u}^1 is the scattered wavefield, and $|\mathbf{u}^1| \ll |\mathbf{u}^0|$. Overall, the scattered wavefield results after summing the response from all single scatter points, but since the scattered wavefield from the inhomogeneity is weak with respect to \mathbf{u}^0 , the wavefields from more scatter points can be negligible (Moradi and Inanen, 2015). This assumption implies that the radiation patterns analysis will not provide information about crosstalk at different spatial locations (Keating and Inanen, 2019).

On the other hand, the isotropic elastic wave equation in time domain for the full displacement wavefield $\mathbf{u}(\mathbf{x}, t)$ is:

$$\rho(\mathbf{x})\ddot{u}_i(\mathbf{x}, t) - \partial_j C_{ij}(\lambda, \mu; u_k) = 0 \quad (5)$$

written for the incident wave as:

$$\rho_0\ddot{u}_i^0 - \partial_j C_{ij}(\lambda_0, \mu_0; u_k^0) = 0 \quad (6)$$

We can find the scattered wave equation by substituting Equation 4 in Equation 5 and using Equation 6, as well as neglecting cross-terms of $(\delta\lambda, \delta\mu, \delta\rho) \times u_i^1$ to only focus on first order perturbations, obtaining:

$$\rho_0\ddot{u}_i^1 - \partial_j C_{ij}(\lambda_0, \mu_0; u_k^1) = \delta f_i(\mathbf{x}, t) \quad (7)$$

The term $\delta f_i(x, t)$ in Equation 7 is a mathematical expression of the interaction between the incident wave and the scatter point (equivalent body force):

$$\delta f_i(\mathbf{x}, t) = -\delta\rho\ddot{u}_i^0 + \partial_i\delta\lambda\partial_j u_j^0 + \partial_j\delta\mu(\partial_i u_j^0 + \partial_j u_i^0) + \delta\lambda\partial_i\partial_j u_j^0 + \delta\mu\partial_j(\partial_i u_j^0 + \partial_j u_i^0) \quad (8)$$

To solve Equation 7, we need to define the equivalent body force according to the type of incident wave we would like to simulate. For a P-wave:

$$\mathbf{u}^{0P} = \mathbf{e}_3 e^{i(k_0 \mathbf{e}_3 \mathbf{x} - \omega t)} \quad \text{where} \quad k_0 = \frac{\omega}{V_{P0}} \quad (9)$$

Then, when u^0 or \ddot{u}^0 appear in Equation 8, the previous expression must be used. Later, the Green's function is applied to solve for the desired type of scattered waves, in this case P-P and P-S. The derivation of u_i^{1PP} and u_i^{1PS} was developed in detail by Sato et al. (2012), producing the following expressions:

$$u_i^{1PP}(\mathbf{x}, t) = \frac{e^{i(k_0 r - \omega t)}}{r} F_i^{PP} \quad (10)$$

$$u_i^{1PS}(\mathbf{x}, t) = \frac{e^{i(l_0 r - \omega t)}}{r} F_i^{PS} \quad (11)$$

where $l_0 = \omega/V_{S0}$ and F_i^{PP} and F_i^{PS} are the scattering amplitudes, which can be written in spherical coordinates as:

$$\mathbf{F}^{PP} = \sum_{i=1}^3 F_i^{PP} \mathbf{e}_i = F_r^{PP} \mathbf{e}_r + F_\psi^{PP} \mathbf{e}_\psi + F_\zeta^{PP} \mathbf{e}_\zeta \quad (12)$$

$$\mathbf{F}^{PS} = \sum_{i=1}^3 F_i^{PS} \mathbf{e}_i = F_r^{PS} \mathbf{e}_r + F_\psi^{PS} \mathbf{e}_\psi + F_\zeta^{PS} \mathbf{e}_\zeta \quad (13)$$

$$F_r^{PP} = \frac{l_0^2}{4\pi} \left[\left(-\frac{1}{\gamma_0^2} + \frac{\cos \psi}{\gamma_0^2} + \frac{2}{\gamma_0^4} \sin^2 \psi \right) \frac{\delta \tilde{\rho}(k_0 \mathbf{e}_r - k_0 \mathbf{e}_3)}{\rho_0} - \left(\frac{2}{\gamma_0^2} \right) \frac{\delta \tilde{V}_P(k_0 \mathbf{e}_r - k_0 \mathbf{e}_3)}{V_{P0}} + \left(\frac{4}{\gamma_0^4} \sin^2 \psi \right) \frac{\delta \tilde{V}_S(k_0 \mathbf{e}_r - k_0 \mathbf{e}_3)}{V_{S0}} \right] \quad (14)$$

with $F_\psi^{PP} = F_\zeta^{PP} = 0$

$$F_\psi^{PS} = \frac{l_0^2}{4\pi} \left[\left(-\sin \psi + \frac{2}{\gamma_0} \cos \psi \sin \psi \right) \frac{\delta \tilde{\rho}(l_0 \mathbf{e}_r - k_0 \mathbf{e}_3)}{\rho_0} + \left(\frac{4}{\gamma_0} \cos \psi \sin \psi \right) \frac{\delta \tilde{V}_S(l_0 \mathbf{e}_r - k_0 \mathbf{e}_3)}{V_{S0}} \right] \quad (15)$$

with $F_r^{PS} = F_\zeta^{PS} = 0$

In Equation 14 and 15, $\gamma_0 = V_{P0}/V_{S0}$. Additionally, each scattering amplitude contains the Fourier transforms of the fractional fluctuations ($\frac{\delta \tilde{\rho}}{\rho_0}$, $\frac{\delta \tilde{V}_P}{V_{P0}}$, $\frac{\delta \tilde{V}_S}{V_{S0}}$) representing the difference between the scattered wavenumber vector and the incident wavenumber vector for an angular frequency. The terms on their left (grouped with parenthesis) are the analytic radiation patterns produced by its associated parameter perturbations.

EXTRACTION OF EMPIRICAL RADIATION PATTERNS

To initially examine the empirical radiation patterns produced by perturbations in P-wave velocity (V_P), S-wave velocity (V_S), and density (ρ), we considered a homogeneous reference medium in each parameter with 200 samples in both x and z directions and with values of $V_P=3000$ m/s, $V_S=1800$ m/s, and $\rho=1400$ kg/m³. Additionally, perturbed media were constructed containing a localized perturbation (scatter point) in one of the three parameters and placed in the middle of the model grid. This perturbation represented an increment of 10% of the respective background value.

The isotropic elastic wave equation in frequency domain was selected as the wave propagation model. An explosive source, represented by a Ricker wavelet with 25Hz of dominant frequency, was located in the middle of the surface of the grid and 1C vertically and horizontally-oriented geophones were placed at each grid point, responding at discrete frequencies and recording the simulated vertical (u_z) and horizontal (u_x) displacement wavefields. Each displacement component was computed twice, (1) simulating that the source wave traveled only in the reference media and (2) simulating that it traveled through the medium perturbed in one parameter class, but with no perturbations of the other parameter classes. The inverse Fourier Transform was applied to each displacement component and the subtraction of the former to the latter displacements corresponded to the scattered wavefield, according to Equation 4, generated by a change in a particular model property (Figure 2).

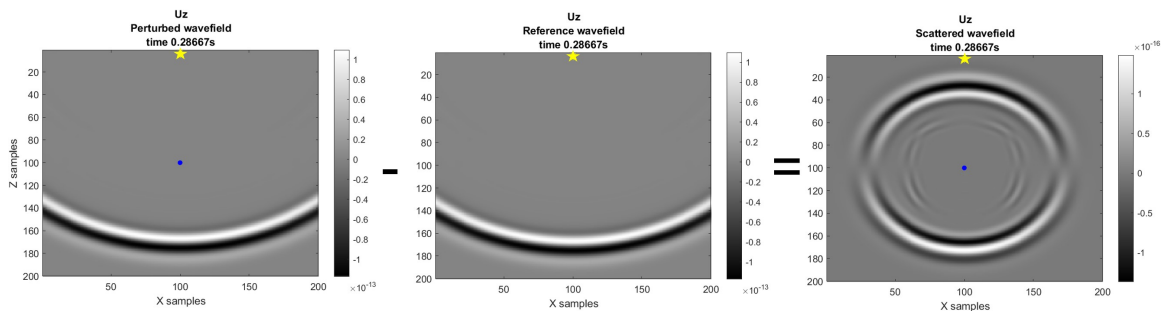


FIG. 2. Mathematical procedure to compute the scattered wavefield caused by a perturbation of one parameter class. The blue dot corresponds to the scatter point, while the yellow star represents the explosive source.

With all the information in time domain, the scattered wavefield was plotted for appropriate times that allowed to visually differentiate both P-P and P-S wavefields. For this fixed time, both types of wavefields were separated using a radius dependent mask of the size of the model grid. Favorable radii were input by the user to isolate both wavefields, considering the values out of the radius when working with P-P energy and within the radius when working with P-S energy (Figure 3).

Later, within the isolated regions, a sweep of angles was performed by fixing a particular angle and selecting a range of 10 discrete upper and lower degrees. The energy within this group of angles was summed and attributed to the fixed angle. The process was repeated for 360 degrees. The energies associated to u_x were summed to those of u_z and the square root was applied so that the total amplitude could be represented. Finally, polar plots were constructed to illustrate the empirical radiation patterns and compared with the

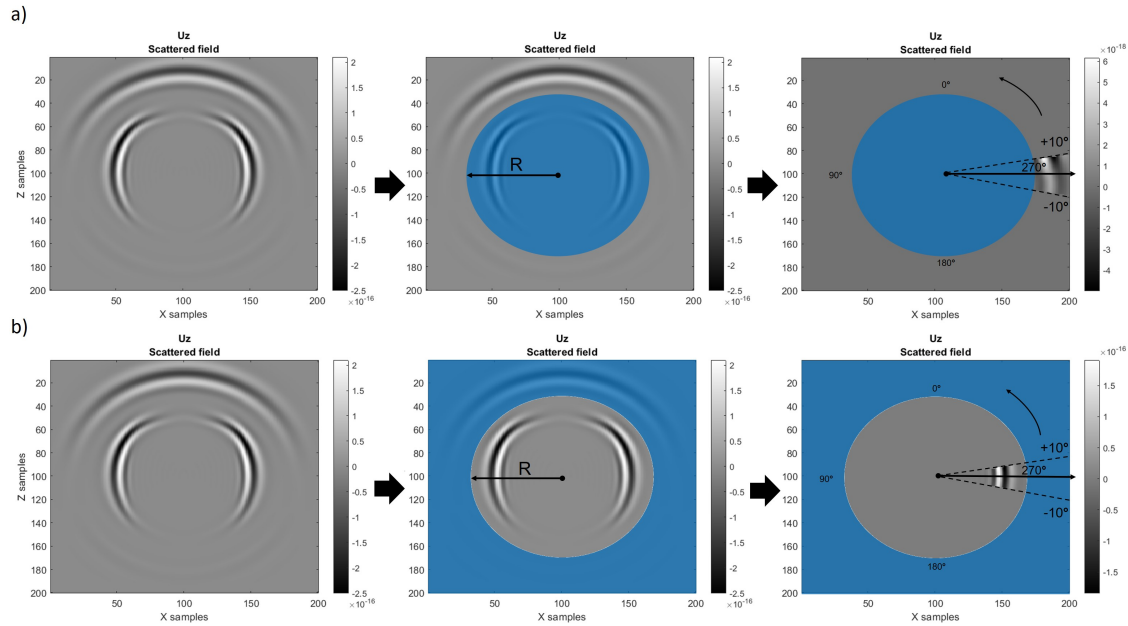


FIG. 3. Proposed workflow to extract the empirical radiation patterns from simulated wavefields. (a) Extraction of patterns from the P-P wavefield. (b) Extraction of patterns from the P-S wavefield. R corresponds to the radius indicated by the user.

obtained from the corresponding analytic expressions.

It is observed in Figure 4 that the shape and values of both, the analytical and empirical, radiation patterns were almost identical for every perturbed parameter class and for each type of energy conversion mode, which means that effectively this workflow recovered accurate enough patterns and can be used in situations where the analytic expressions are unknown.

RADIATION PATTERNS WITH HETEROGENEOUS REFERENCE MEDIA

Three different heterogeneous background media with varying complexities were studied using the procedure described in the previous section. The first case consisted in reference media for V_P , V_S , and ρ with a linear increment of values with depth; the second case corresponded to a linear increment of values with depth, but with an increment of 25% of the slopes of the first case; and the third case was a modified Marmousi model (the original V_P Marmousi model was divided by 2 to obtain V_S and by 1.5 to obtain ρ). Figure 5 illustrates the perturbed V_P medium in each case. Once more, for each of these scenarios, scatter points were placed in the middle of the grid with values of 10% increment with respect to the reference media.

For each case, the model size was modified to avoid grid dispersion effects. Figures 6 and 7 show a comparison between the analytic radiation patterns, those obtained from a homogeneous background, and those obtained after considering the heterogeneous reference media proposed in this section. In that sense, for the cases of heterogeneous background, the general shape of the scattering patterns prevailed, but some changes appeared in terms of rotation of lobes and amplitude ratio.

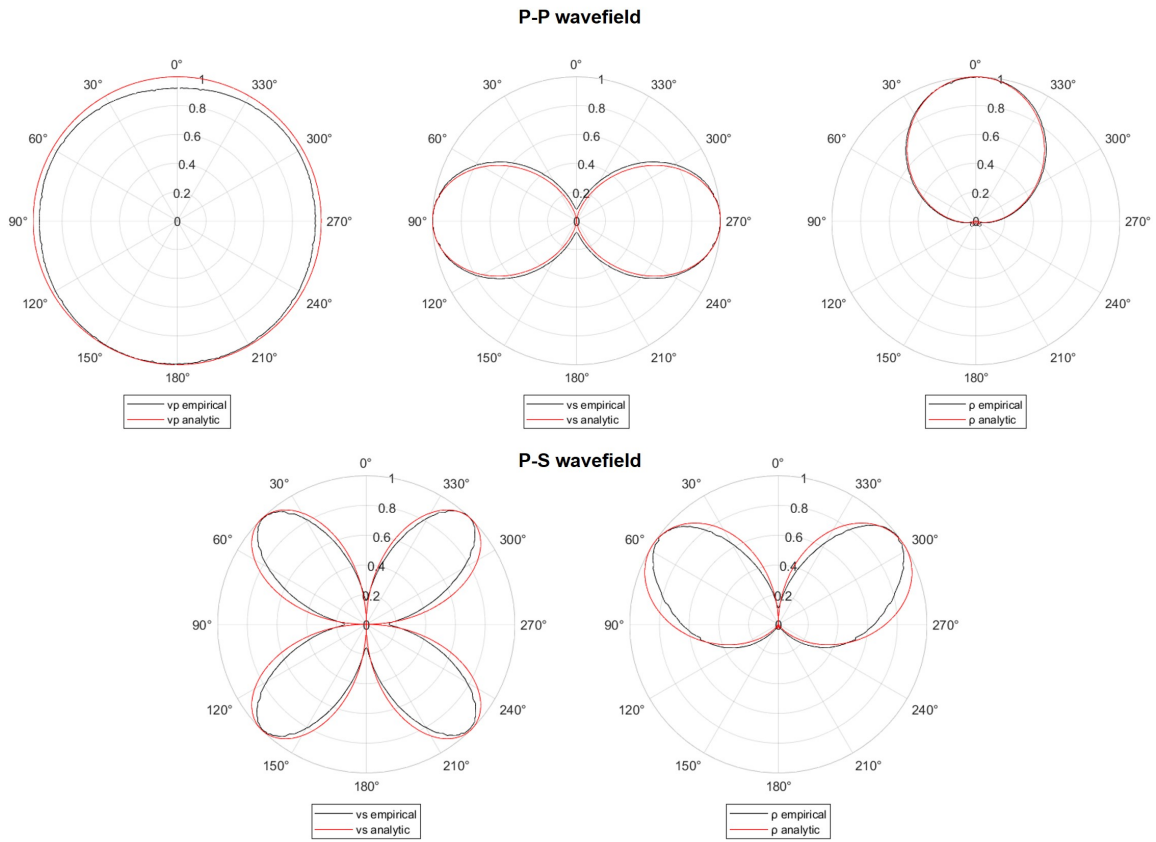


FIG. 4. Comparison between analytic and empirical radiation patterns of P-P and P-S wavefields.

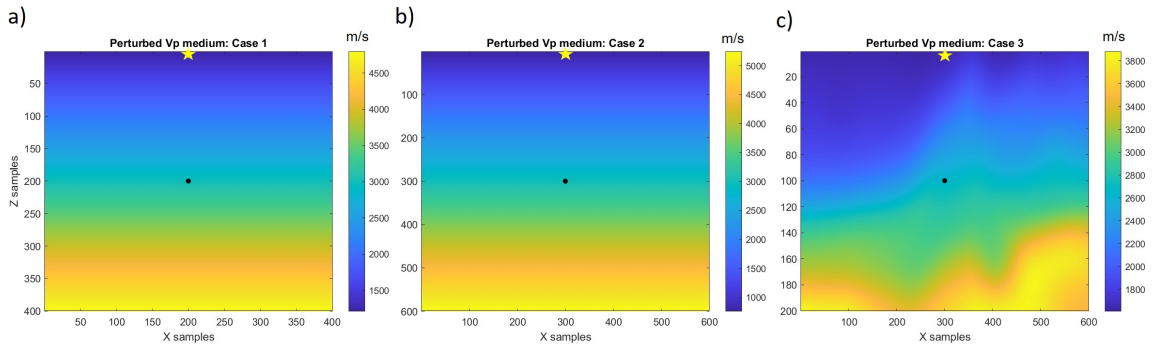


FIG. 5. Different heterogeneous reference media used in this study. (a) Case 1, (b) case 2, and (c) case 3.

When values of the reference media increase linearly with depth (case 1 and 2), scattering amplitudes tended to be more focused around smaller angles than those described by the analytic responses. For instance, there was a slight upward rotation of the radiation lobes associated to changes in ρ for the P-S wavefield and V_S for the P-P and P-S wavefield. Additionally, the V_P scattering pattern (P-P wavefield), even though still circular, did not have its characteristic analytic isotropic behavior anymore, but higher amplitudes were scattered towards small and intermediate angles. Moreover, the radiation pattern caused by ρ perturbations (P-P wavefield) shrank mainly towards small angles.

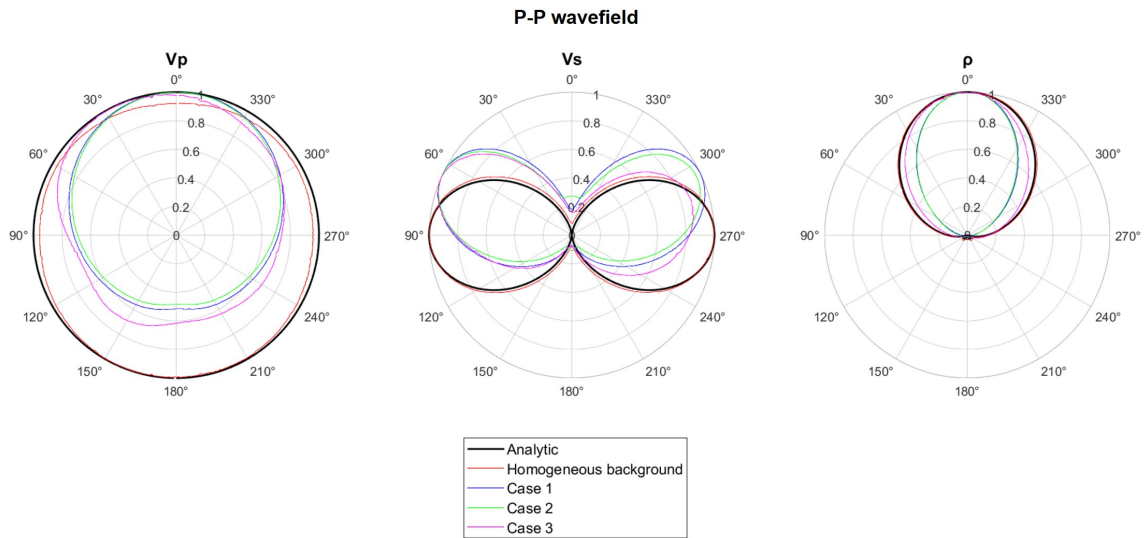


FIG. 6. Overlapped radiation patterns of analytic, homogeneous, and heterogeneous cases extracted from the P-P wavefield.

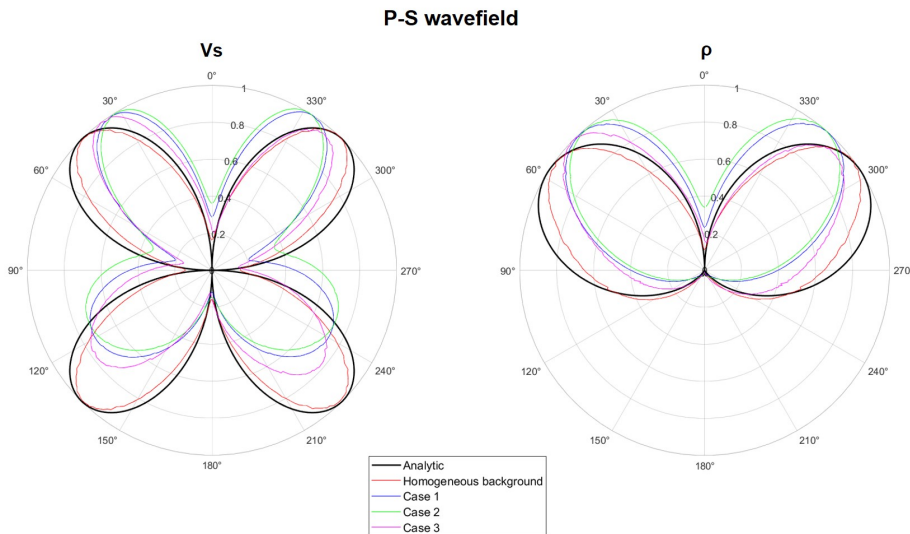


FIG. 7. Overlapped radiation patterns of analytic, homogeneous, and heterogeneous cases extracted from the P-S wavefield.

On the other hand, areas with increment of values with depth and structural complexities, represented by the modified Marmousi model (case 3), exhibited radiation patterns with behaviors in between the homogeneous case and case 1-case 2, and the shape of the patterns differed with respect to the analytic shapes for some angles. Hence, rotation of lobes still occurred similar to the previous heterogeneous cases, but especially for the P-P wavefield and the V_P and ρ patterns, the amplitude values tended to get closer to those described by the analytic expressions. Therefore, the shrinkage of the ρ radiation pattern was much more subtle and the V_P radiation pattern had higher amplitudes scattered from small to large angles, but it lost its perfectly circular isotropic shape.

Figure 8 and 9 illustrate the overlapped scattering patterns of each parameter perturbation generated by the analytic and empirical procedures. For the P-P wavefield, the analytic

V_P and ρ patterns indicated crosstalk in very small angles (0-6°), and for the heterogeneous cases the crosstalk occurred in slightly smaller angles, with lack of symmetry for the Marmousi reference media. Regarding the comparison between V_P and V_S radiation patterns, crosstalk in case 2 was the least similar to what was expected from the analytic responses, with no crosstalk in large angles but in very small ones. Moreover, according to the analytic expressions, no crosstalk should appear between parameters V_S and ρ , but for case 3 a small overlap of the patterns existed between 80 and 90°. For the P-S wavefield, the analytic expressions of V_S and ρ suggested crosstalk from 0 to almost 30° and its counterpart; however, case 1 and 3 showed overlap of the radiation patterns from 0 to 20° and for case 2, from 0 to 5°.

Therefore, subtle differences existed between the crosstalk indicated by the analytic and the empirical patterns and, in some cases of the P-P wavefield, new small crosstalk regions appeared. However, the empirical patterns also gave insights on the strong variations of amplitude values that effectively occur between patterns of each case, which suggest that sensitivity issues might be present during the inversion depending on the considered reference media.

CONCLUSIONS

Simulated scattered wavefields allowed to introduce a workflow to isolate the P-P and P-S mode energy conversion and extract their empirical radiation patterns with high accuracy, which is beneficial to perform crosstalk analysis in heterogeneous configurations or using re-parameterizations where the analytic expressions are somehow unknown. This workflow demonstrated that the shape of the radiation patterns generated from heterogeneous reference media is very close to the indicated by the analytic expressions, but in some cases, rotation of lobes, decrease of amplitude values, and loss of symmetry or irregularities might occur. Moreover, the overlap of these heterogeneous scattering patterns helped to perform more accurate analysis under more realistic scenarios, since the produced crosstalk between parameters might slightly change with respect to those indicated by the analytic expressions and different sensitivities between patterns might be present, having impact on the inversion of the observed data.

ACKNOWLEDGMENTS

The authors would like to thank the sponsors of the CREWES project as well as the NSERC (Natural Science and Engineering Research Council of Canada) under the grant CRDPJ 543578-19 for making this work possible through their financial support.

REFERENCES

- Kamath, N., and Tsvankin, I., 2016, Elastic full-waveform inversion for vti media: Methodology and sensitivity analysis: *Geophysics*, **81**, No. 2, C53–C68.
- Keating, S., and Innanen, K., 2019, Parameter cross-talk and leakage between spatially-separated unknowns in viscoelastic full waveform inversion: *CREWES Research Report*, **31**, No. 35.
- Moradi, S., and Innanen, K., 2015, Radiation patterns associated with the scattering from viscoelastic inclusions: *CREWES Research Report*, **27**, No. 53.
- Moradi, S., and Innanen, K., 2019, Azimuthally-dependent scattering potentials and full waveform inversion sensitivities in low-loss viscoelastic orthorhombic media: *Journal of Geophysics and Engineering*, **16**, 367–388.
- Métivier, L., Brossier, R., Operto, S., and Virieux, J., 2015, Acoustic multi-parameter FWI for the reconstruction of p-wave velocity, density and attenuation: preconditioned truncated newton approach: *SEG Expanded Abstracts*, 1198–1203.
- Operto, S., Gholami, Y., Prieux, V., Ribodetti, A., Brossier, R., Métivier, L., and Virieux, J., 2013, A guided tour of multiparameter Full-Waveform Inversion with multicomponent data: From theory to practice: *The Leading Edge*, 1040–1054.
- Sato, H., 1984, Attenuation and envelope formation of three-component seismograms of small local earthquakes in randomly inhomogeneous lithosphere: *J. Geophys. Res.*, **89**, 1221– 1241.
- Sato, H., Fehler, M. C., and Maeda, T., 2012, *Seismic Wave Propagation and Scattering in the Heterogeneous Earth*: Springer, 2 edn.
- Wu, R. S., and Aki, K., 1985, Scattering characteristics of elastic waves by an elastic heterogeneity: *Geophysics*, **50**, 582–595.

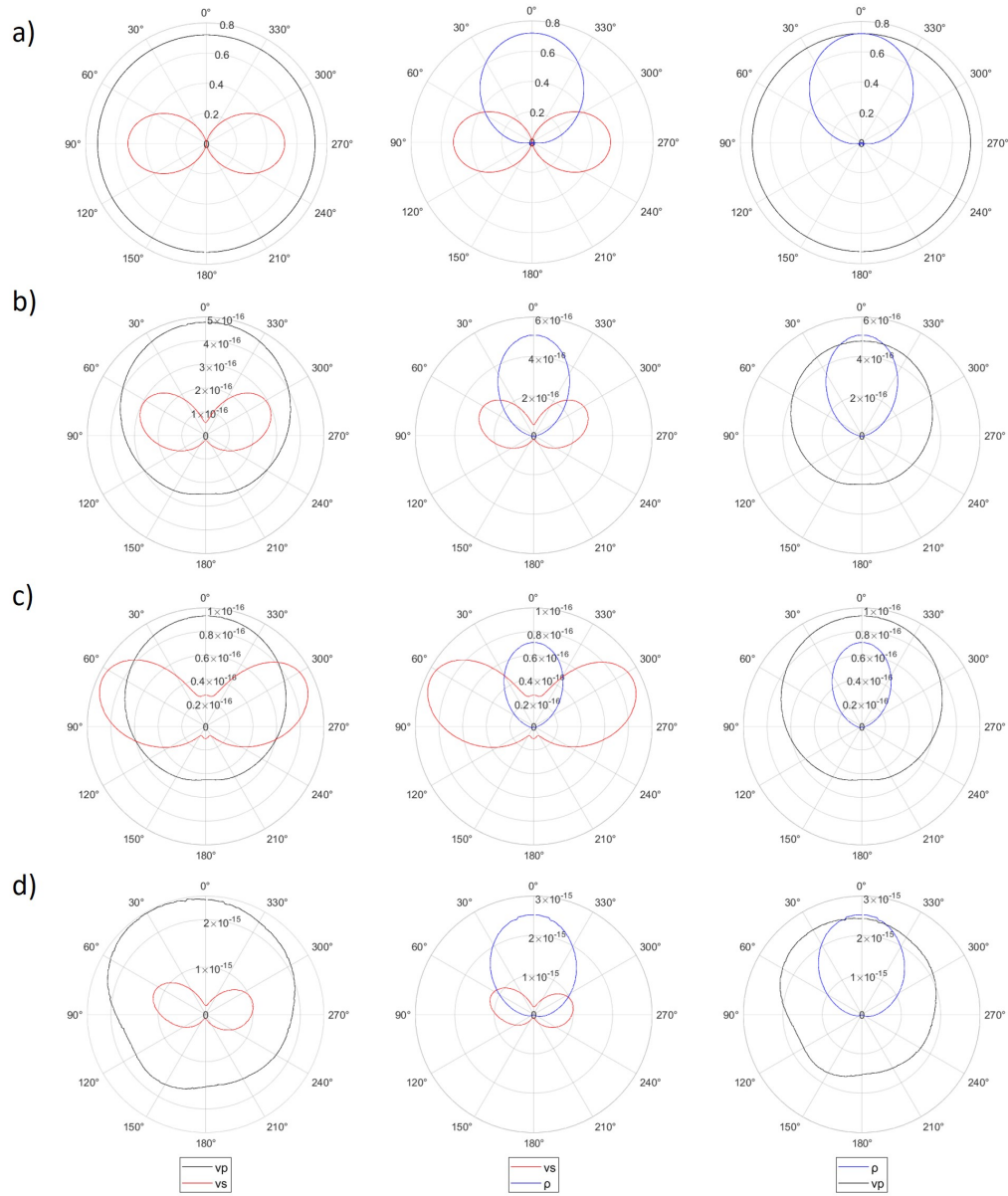


FIG. 8. Crosstalk assessment with radiation patterns extracted from P-P wavefield. (a) Analytic expressions, (b) case 1, (c) case 2, and (d) case 3.

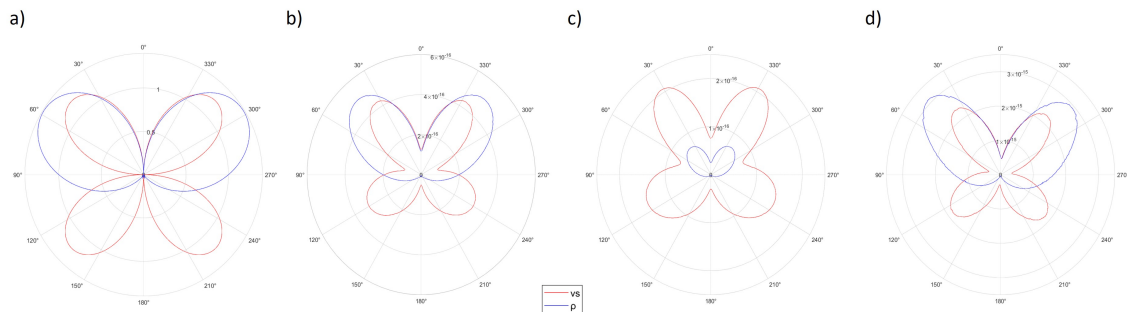


FIG. 9. Crosstalk assessment with radiation patterns extracted from P-S wavefield. (a) Analytic expressions, (b) case 1, (c) case 2, and (d) case 3.